

Realization of Pristine and Locally-Tunable One-Dimensional Electron Systems in Carbon Nanotubes

J. Waissman, M. Honig, S. Pecker, A. Benyamini, A. Hamo and S. Ilani

- S1. Local cutting of the suspended NT**
- S2. Images of additional devices**
- S3. Details of the electrostatic calculation**
- S4. Quantitative estimate of electronic disorder strength**
- S5. Electrostatic analysis of the gate-gate conductance scans**
- S6. Designing electrostatic potentials with resolution determined by the gate pitch**
- S7. Transport data of a second device at dilution refrigerator temperatures**
- S8. Electrical functionality of the two-NT device as a coupled system-detector**

S1. Local cutting of the suspended NT

After the circuit is mated to a NT and *in-situ* transport measurements show the NT is clean and has the desired bandgap, we typically want to separate the device chip from the NT chip to allow transferring the prepared device for measurement in other setups. We achieve this separation by controlled cutting of the NT at well-defined positions, as explained in detail below.

The process is demonstrated in Figure S1a, which shows an SEM image of a seven-gated suspended NT device that has been selectively cut at two places (a magnified top-down view of these cuts is shown in the insets; the cuts are indicated by arrows). The relevant device segment is at the center, above the gates. To enable cutting at various locations we fabricate several contacts at each side of the device. The cutting process consists of applying a voltage between two adjacent contacts, which drives a large current through the short suspended NT segment between them. When the current passes a

critical threshold the NT breaks at a single point, close to the center of the suspended segment. This cutting is believed to be due to Joule heating that leads to the highest temperature near the center of the suspended segment, which is farthest from the contacts that dissipate the heat.

The line traces in the insets of Fig S1a show the current-voltage characteristics measured during the cutting. As a function of the applied voltage the current grows monotonically, until reaching the critical current ($15\mu\text{A}$ - $30\mu\text{A}$) and then dropping abruptly to zero, indicating that the segment between the contacts was cut. Measurement of transport through NT segments adjacent to the one that was cut before and after its cutting shows that they remain unaffected by this local process. Another technique that was found to efficiently cut the NT locally is the application of fast voltage pulses (typically $\sim 10\text{Volts}/0.5\mu\text{s}$) to one contact while its neighbor contact is grounded and all other contacts are floating. However, we generally prefer to do the cutting using the first approach (DC current) since it further allows us to distinguish between an individual single-wall NT vs. bundles or multi-wall NTs. For the latter, the cutting does not happen in a single step, but often exhibits multiple steps that correspond to the multiple tubes or multiple shells breaking one at a time. An example of such a two-stepped cut is shown in Fig. S1b. We observe the same pattern of steps when cutting the same NT at different junctions, demonstrating that these reflect the intrinsic properties of the tube and not of the junctions. If upon the first cut we observe any indication of a bundle or multiple shells we detach the circuit from the NT before performing the second cut and move to mate with a different tube. In general, we choose the growth parameters to yield sparse growth of suspended NTs, thereby avoiding bundles. However, if we find, using the above measurements, that a specific chip has a high density of NTs or indications of bundles we discard it.

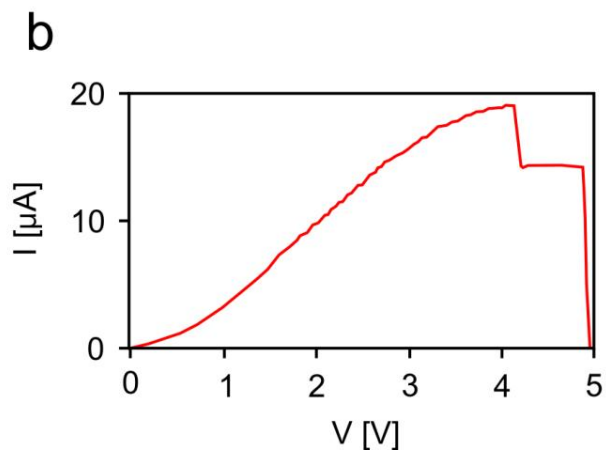
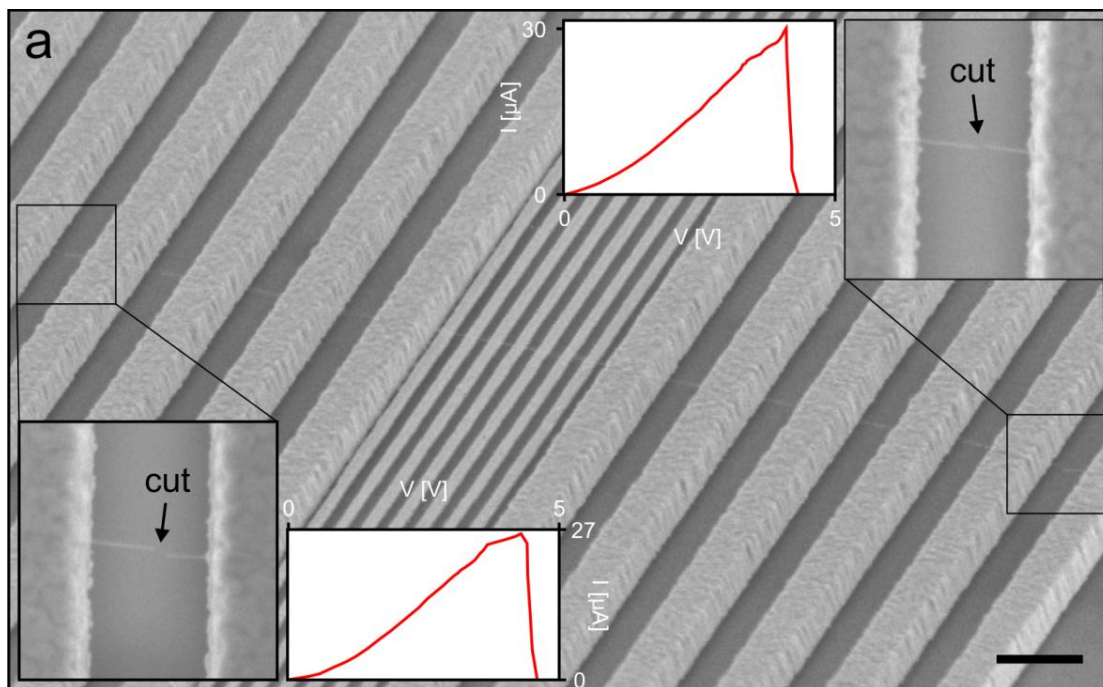


Figure S1: The selective NT cutting process. a) Main panel: Scanning electron micrograph of a seven-gated suspended NT device. Top-right and bottom-left insets: magnified top-down views of suspended segments that were cut using Joule heating with a flow of current (see text). The cut position is indicated by an arrow. Top right and bottom left traces: I - V curves of the burning process during voltage ramp-up. b) A cutting I - V curve during voltage ramp-up showing two abrupt current drops, attributed to the presence of a two-NT bundle or a double-walled NT.

S2. Images of additional devices

In this section we show scanning electron microscope (SEM) images of three multi-gate devices formed using the mating technique, different than that shown in Figure 2c and d of the main text. Devices 2 and 3 have seven local gates, while Device 4 has five gates. These SEM images show that the NTs are anchored across the entire length of the contacts, are straight, and remain suspended above the gates with no slack, similar to the device shown in the main text. In fact, we find the vast majority of the devices made by our nano-assembly technique to have these ideal geometric features.

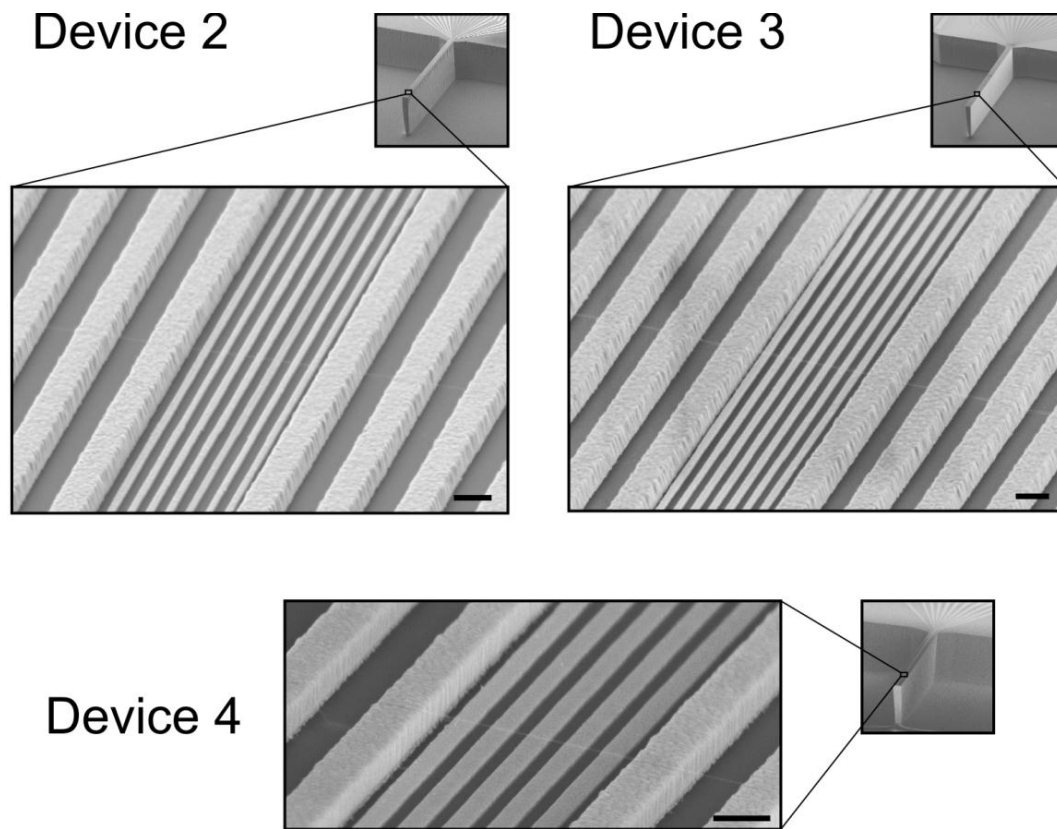


Figure S2: Robustness of the mating technique: additional devices. Scanning electron micrographs of circuits mated to suspended NTs (all scale bars = 300 nm). All devices underwent the cutting process, and all NTs remained intact and suspended over the gates, as shown. Devices 2 and 3 have seven gates of 65 nm width and 85 nm spacing. Device 4 has five gates of 120 nm width and 80 nm spacing.

S3. Details of the electrostatic calculation

An important feature of the 1D multi-gated NT systems we present in this work is the ability to engineer any 1D potential profile along the NT length. Naively, the simplest way to create a potential $\phi(x)$, where x is the position along the NT, is to have gates as close as possible to the NT such that their gating is local and their voltages directly determine $\phi(x)$. However, close proximity to metallic gates screens the interactions between electrons in the NT, thus destroying this salient feature. We therefore intentionally choose to distance the gates from the NT, the price being that gating becomes non-local, and a gate influences not only the NT segment above it but also segments above other gates. Knowing what gate voltages are required to produce a certain $\phi(x)$ thus necessitates quantitative knowledge of the non-local capacitive coupling to the NT. In Fig. 4 of the main text we show that we can extract this coupling directly from measurements with localized quantum dots, and that it corresponds quantitatively well to calculations, with no free parameters. In this section we explain in detail how the measurements of local quantum dots are translated to the spatial capacitance distribution of the gates, and the details of the finite element calculations.

The influence of a specific gate on the NT is fully captured by a capacitance distribution function $C_i(x) = en(x)/V_{gi}$, where e is the electron charge, i is the gate index and $n(x)$ is the charge distribution along the NT induced by a gate voltage V_{gi} , under the assumption that the NT is a perfect metallic conductor. We are interested in a discretized version of this function where the NT is partitioned to N segments of equal length l (N is the number of gates) each segment being positioned above a corresponding gate. This partitioning reflects the “effective resolution” with which we can define the potentials with the gates. The capacitance of a gate i to a segment j is then given by $C_{ij} = \int_{segment\ j} C_i(x) dx \approx C_i(x_j) \cdot l$, where x_j is the center coordinate of the segment. Experimentally we can extract a closely related quantity, by measuring the charge response of a quantum dot localized at position j to the voltage on gate i . The latter amounts to $\tilde{C}_{ij} = \int_{dot\ j} C_i(x) dx \approx C_i(x_j) \cdot l_{dot\ j}$, where $l_{dot\ j}$ is the length of the dot formed at position j . Clearly, the \tilde{C}_{ij} 's depend on the shape of the quantum dots.

However, if we take only their ratios that measure the response of the *same* dot to two different gates, the details of the dot cancel out and we remain with the ratios of the quantities that we are seeking : $C_{ij}/C_{ii} = \tilde{C}_{ij}/\tilde{C}_{ii}$. These capacitive coupling ratios are directly extracted from the slope of the charging lines in the two-gate conductance scans shown in the multiple panels of figure 4 in the main text.

The ratios above give only relative capacitances, and thus do not provide the full information needed to determine all the absolute capacitance elements in the C_{ij} matrix. To get the missing information we complement these data with measurements of the integrated capacitance of individual gates. To obtain these we form a large quantum dot extended over the entire suspended NT. We first measure the total capacitance of this dot to all five gates chained together. This quantity is directly extracted from the gate periodicity of the Coulomb oscillations in figure 3a of the main text. This capacitance gives the sum of all the C_{ij} matrix elements: $C_{total} = \sum_{ij} C_{ij}$. Then we measure the relative contribution of each of the gates to this capacitance, giving the sum of one row in this matrix, $C_i/C_{total} = \sum_j C_{ij}/C_{total}$. We get the latter by comparing the width of a Coulomb peak of the large dot when only one gate is scanned vs. the width of this peak when all gates are scanned. Together, all these quantities give us the full capacitance matrix without any free parameters.

The electrostatic simulations are performed with the finite-element calculation package COMSOL. For this, we use the real device dimensions extracted from SEM images to model the geometry. This includes the trapezoidal cross-section of the contacts, arising due to gradual closing of the e-beam resist window during the thick evaporation. The electrode and substrate geometry that go into the calculation are shown in the bottom inset of Fig. 4 of the main text. We model the nanotube as a metallic cylinder resting on the contacts and suspended over the gates. To extract the capacitance distribution of gate i we set the voltage on this gate to V_{gi} while keeping the other gates, the contacts and the NT grounded. We then calculated the resulting charge distribution along the NT, $n(x)$, from which we get directly the capacitance distribution of this gate, $C_i(x) = en(x)/V_{gi}$. These capacitance distribution functions for the individual gates are shown in Fig. 4 of the main text, matching the experimental values with no free parameters.

S4. Quantitative estimate of electronic disorder strength

As will be explained below, with the multiply-gated devices we can not only set the potential profile with the gates, but also estimate its magnitude in the absence of gating. The latter, which corresponds to the uncontrolled disorder potential fluctuations in our device, therefore provides an experimental estimate for the strength of disorder on length scales set by the gates' resolution. Our goal is thus to measure the uncontrolled potential modulations, $\delta\phi(x)$, that exist in the NT in the absence of gating.

If the NT had the same work function as the gate metal, it would be un-gated when all the gates are un-biased with respect to the NT ($V_{gi,i=1..5} = 0$). However, since generally these workfunctions are different, the absence of *electrochemical* bias on the gates ($V_{gi,i=1..5} = 0$) actually means that there is a non-zero *electrostatic* potential difference between the gates and the NT. This difference, termed the “contact potential”, amounts to $\delta W_{gate-NT} = W_{gate} - W_{NT}$, and it gates the NT. To null this gating one must therefore apply a canceling electrochemical bias to the gates, $V_{gi,i=1..5} = -\delta W_{gate-NT}$. It is important to note that the contacts, which are by definition electrochemically shorted to the NT, produce a similar gating effect due to the difference between their workfunction and that of the NT, $\delta W_{contact-NT} = W_{contact} - W_{NT}$. This is the reason for the large hole doping of the NT segments that lie on top of the contacts, mentioned in the main text.

Combining the above understanding with finite element simulations, which were shown in the previous section to describe our system quantitatively well, we can determine the bare electrostatic potential produced along the NT for any combination of gate voltages:

$$\phi(x) = \sum_i \alpha_i(x) \cdot (V_{gi} + \delta W_{gate-NT}) + (\alpha_S(x) + \alpha_D(x)) \cdot \delta W_{contact-NT}, \quad \text{Eq. S1}$$

Here $\alpha_i(x)$, $\alpha_S(x)$ and $\alpha_D(x)$ are unit-less functions, determined from the finite elements simulations, that give the potential along the NT per unit of voltage applied on gate i , the source and the drain respectively. The *a priori* unknown work function differences, $\delta W_{gate-NT}$ and $\delta W_{contact-NT}$, are the two free parameters of this equation that are determined from the experiments (see below).

To elucidate the relation between the potential profiles given by Eq. S1 and the measured transport we take as an example the top conductance trace from Fig. 3b in the main text that corresponds to the formation of a quantum dot above gate 1 (reproduced in Fig. S3a). In this scan V_{g1} is swept while all the other gates are kept at fixed voltages $V_{g2..5} = -0.8V$. The calculated potential profiles, $\phi(x)$, that correspond to three gate voltages along this scan (circles in Fig S3a) are shown in Fig. S3b (work function differences are included; see below). In each of these plots the $\phi(x)$ in the suspended segment corresponds to the center of the NT bandgap as a function of position. Wherever it crosses from below to above the Fermi energy, E_F (dashed horizontal line), the local occupation changes from holes to electrons.

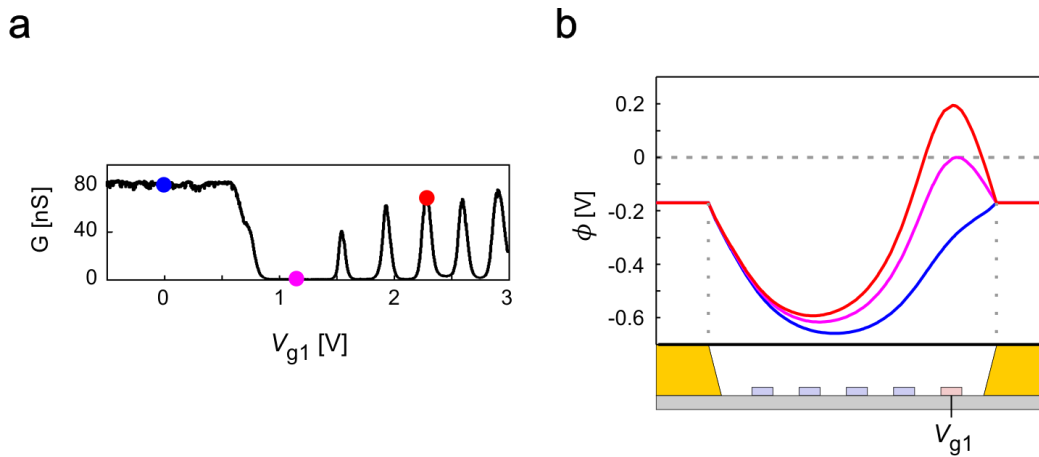


Figure S3: Calculated bare electrostatic potential profiles along the NT for three different gating configurations. a) Measured conductance trace for a dot formed above gate 1, equivalent to the top trace in figure 3b of the main text. In this measurement V_{g1} is swept while the rest of the gates have a fixed potential $V_{g2..5} = -0.8V$ that dope the segment above them with holes. b) Three calculated potential profiles calculated using finite elements and Eq. S1, corresponding to three different transport regimes (the corresponding V_{g1} 's are shown in panel a as dots with similar colors). Workfunction differences are included (see text).

At low V_{g1} the corresponding $\phi(x)$ (blue trace) is at all positions below E_F , implying that the NT is populated with holes over its entire length, thus forming a continuous “NT wire”. At high V_{g1} , the corresponding $\phi(x)$ (red trace) exceeds E_F above gate 1, crossing it at two points. At these points p - n junctions form, confining the electrons above gate 1 to a quantum dot. In between these regimes there is a $\phi(x)$ that exactly reaches E_F above

gate 1 (purple trace). For this potential the center of the NT bandgap is at E_F above gate 1, forming a single long barrier above this gate. This point corresponds to the center of the non-conducting regime in the transport (purple point Fig S3a) where the conductance is maximally suppressed.

Looking at the corresponding transport traces obtained by scanning the other local gates (Fig S4a, reproduced from Fig 3b) we see that the center of the “gap” appears at very different gate voltages for the different gate positions. Fig S4b plots the gap-center gate-voltage as a function of the gate position, showing that this value changes by $\Delta V_g \approx 325mV$ from the side gate to the center gate. This seemingly large potential modulation is in fact a direct result of the position dependence of the device electrostatics combined with the finite workfunction difference between the gates/contacts and the NT. Both these effects should be fully captured by Eq. S1. Thus, if this equation is accurate, in the absence of disorder we should be able to reproduce the position of these five gap centers, with just two parameters (the metal workfunctions). This is demonstrated in Fig. S4c, where we show the five $\phi(x)$'s that correspond to the gap centers in the five different conductance traces, calculated with $\delta W_{gate-NT} = -40mV$ and $\delta W_{contact-NT} = -170mV$. These work function values are consistent with published values for gold, palladium, and carbon NTs. We can clearly see that in all cases the potential reaches E_F above the corresponding gate with an accuracy of $\delta\phi \approx \pm 5mV$. These small fluctuations compared to those observed in Fig S4b ($\Delta V_g \approx 325mV$) show that most of the effect is a consequence of the device electrostatics, and once it is known quantitatively it can be taken into account and nulled out. The remaining small fluctuations give us an upper bound of $\sim 5mV$ on the magnitude of the bare potential disorder on the length scale set by the gate width. Using the lever-arm of the local gates ($\alpha \sim 0.3$) this is translated to $\sim 17mV$ on a local gate, and by comparing this to the measured single-gate Coulomb blockade periodicity ($\Delta V_g \sim 315mV$) necessary to introduce an electron charge above a gate we can obtain an upper bound on the local charge disorder of $\delta n \sim 5 \cdot 10^{-2}e$ on the gate length scale, a small fraction of a single electron charge. Alternatively, we can consider the induced fluctuations in the self-consistent disorder potential, where screening will reduce the bare disorder potential seen

by electrons. By factoring in the ratio between the geometric capacitance ($\sim 4aF/\mu m$) and the quantum capacitance ($\sim 400aF/\mu m$) of the nanotube, we estimate the self-consistent disorder potential at $\sim 50\mu V$. We note that this is a strict upper bound, since the potential fluctuations that we consider include all the errors in the measurements and calculations. The actual disorder is most likely significantly smaller. We also note that potential fluctuations on smaller length scales, which are too weak to form barriers for electron transport at the temperature of our measurements, would not be observed here.

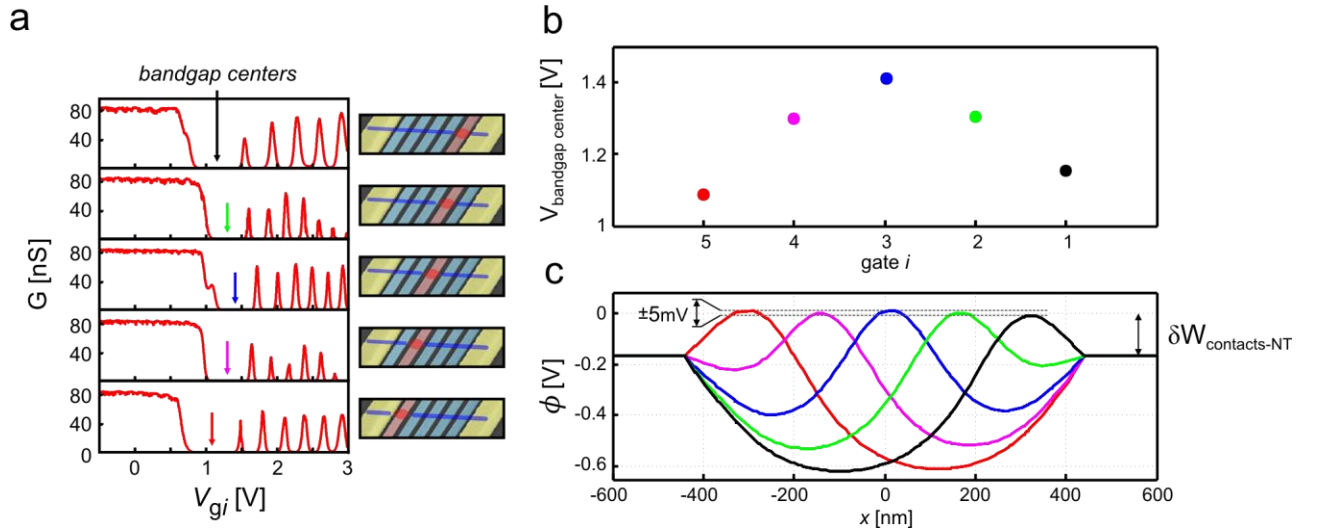


Figure S4: Extracting an upper bound on the disorder potential from the measured transport. a) The single-gate conductance scans reproduced from Fig 3b of the main text with the bandgap centers marked by colored arrows corresponding to the colored points in panel b and colored curves in panel c. b) The gap-center voltage as a function of the gate index, extracted from the graphs in panel a. c) The bare electrostatic potentials along the NT, $\phi(x)$, calculated using Eq. S1 for the gate voltage configurations that correspond to the positions indicated by the respective arrows in panel a, with $\delta W_{gate-NT} = -40mV$ and $\delta W_{contact-NT} = -170mV$. Although the gate voltage at the gap center varies between dots at different locations by as much as $\sim 325mV$, when we take into account the electrostatics of the device through Eq. S1 we see that within $\delta\phi = \pm 5mV$ all the potential profiles corresponding to the center of the gap are at the Fermi energy, giving an upper bound for the residual bare disorder potential fluctuations.

S5. Electrostatic analysis of the gate-gate conductance scans

In this section, we analyze the features observed in the conductance map of Fig. 3c (and its symmetric partner in Fig. 3d). We use the electrostatic understanding established in section S3 and S4 above to determine the potential landscapes formed along the NT at

the various gating configurations which correspond to different points in Fig. 3c and use these profiles to demonstrate the underlying sources of the observed features.

In figure S5a we reproduce Fig. 3c of the main text and highlight the secondary conductance features that are observed on top of the Coulomb blockade features described in the main text. The first set of features, apparent in this scan and its symmetric partner (Fig. 3d), are stripes of conductance modulation that are marked by dashed black lines. These stripes cross through the Coulomb charging lines and modulate their peak heights. The electronic configuration which corresponds to this region in the gate-gate diagram consists of an electron dot formed over gates 1 and 2 (red in device schematics) while above gates 3 to 5 the NT is populated with holes (blue in device schematics). The hole population in this segment is continuously connected to the holes above the left contact, forming a continuous “hole wire” that acts as a “NT lead” for the electronic quantum dot. We can confirm this picture by calculating the electrostatic potential induced by the gate voltages as shown in Fig.S4b, where the NT lead and the electron dot correspond to the potential well and hill above their respective gates. By calculating the potentials at two points along the modulation stripe (indicated in the figure by red and blue circles), we see that the potential well corresponding to the NT lead remains identical while only the electron potential hill has changed. This indicates that going along a stripe preserves the charge density in the NT lead, whereas going perpendicular to it changes this charge density. Thus, the origin of the observed striped modulations of the Coulomb peak heights is reproducible Fabry-Perot-like modulation of the conductance of the “NT lead” (the nature of these conductance modulations is discussed further in the last paragraph of this section).

We now proceed to confirm this picture with a calculation of the stripe slopes. Although gates 1 and 2 are far from the NT lead, they still gate it by an amount that can be quantitatively determined from the capacitance distribution functions which were measured and calculated (inset for Fig 4 in the main text). The relative capacitance of the two gates to the NT lead amounts to the ratio of the areas under the capacitance distribution curves of these two gates integrated over the length of the NT lead, as shown in Fig. S5c. The edge of the hole occupation is determined from the point where the

electrostatic potential $\phi(x)$ crosses zero, since this is where the p - n junction barrier will be centered. In the discretized version these capacitances are given by the elements of the capacitance matrix, $C_1^{p\text{-lead}} = C_{13} + C_{14} + C_{15}$ and $C_2^{p\text{-lead}} = C_{23} + C_{24} + C_{25}$, all of which we measure directly. The dashed black lines in figure S5a are drawn with a slope $C_1^{p\text{-lead}}/C_2^{p\text{-lead}}$ taken from these measurements, showing a good fit to the observed conductance modulation slopes.

Another clear feature observed in the two, mirror-symmetric, gate-gate scans is a band of suppressed conductance (dashed white lines, Fig S5a). We calculate the electrostatic potential in the middle of this suppressed band along the same line of fixed NT lead gating, shown in green in Fig. S5b. From the electrostatic calculations we can identify that this feature corresponds to having the electron dot confined over only a single gate (gate 2) and having the NT bandgap pinned between gate 1 and the right contact. In this case, the right tunnel barrier of the electron dot is a p - n junction formed above an edge gate (gate 1 or gate 5), which has a longer depletion length than when formed above a center gate because the nearby contact is grounded (as opposed to the negatively-biased gates). The underlying origin of the longer barrier is the shallower slope of $\phi(x)$ where intersects zero on the right. The existence of this extended edge barrier explains the observed conductance suppression. The slope of the dashed white line in the conductance map that follows the middle of the observed suppression band is $\frac{\Delta V_2}{\Delta V_1} \approx 2.5$, corresponding reasonably well to that calculated with the capacitance distributions, $C_1^{p\text{-}n\text{ barrier}}/C_2^{p\text{-}n\text{ barrier}} \approx C_{11}/C_{12} = 2.3$. We note here that the actual length of the p - n junction will depend on electrostatic and quantum effects, and determining it requires a full solution of the Schrodinger-Poisson self-consistent equations. However, we are interested only in the positions of features in the voltage-voltage plane, which depend on the position of the p - n junction (and not its width), and this is captured well by our analysis.

Continuing to the other side of the suppression feature, the calculated electrostatic potential (gray line, Fig. S5b) shows that the quantum dot remains over gate 2, but above gate 1 there is now a hole population, showing that the right “NT lead” has extended over

gate 1. As a result, the right p - n junction is now shorter and the conductance is higher, comparable to that on the other side of the suppression feature.

Finally, we would like to comment on the nature of the hole-doped “NT leads” to the electronic dot. In the main text we mentioned that when the NT is populated entirely with holes it behaves like a “NT wire”. In this regime we measure only weak gate modulation of the conductance, which phenomenologically resembles the measurements of NTs in the Fabry-Perot regime¹. In that regime the barriers between the NT and the contacts are highly transparent and the average conductance is comparable to $4e^2/h$. In our case, on the other hand, the measured conductance is significantly smaller than the quantum conductance and thus one expects the NT to behave as a quantum dot rather than a Fabry-Perot cavity. This dot, however, is unusual since its charging energy is strongly suppressed. This suppression results from the fact that the NT sits directly over the contacts and thus has an extremely large capacitance to them. At such short distances the geometrical capacitance to the contact, $C_{source}^{geometrical}$, is much larger than the quantum capacitance of the NT segment above it, $C_{source}^{quantum}$, so that the latter dominates the total source capacitance, which in our case is $C_{source} = [C_{source}^{geometrical}{}^{-1} + C_{source}^{quantum}{}^{-1}]^{-1} \approx 100aF$. The resulting charging energy of the NT leads, $U = e^2/(C_{source} + C_{drain} + \sum C_{gates})$, being dominated by C_{source} , thus roughly equals the level spacing of the NT above the contacts. In this respect, the system is similar to the Fabry-Perot cavity. The large suppression of the charging energy as compared to the quantum dots on the suspended part of the NT explains why at $T = 4K$ the hole-doped NT behaves similarly to a Fabry-Perot cavity and shows weak Coulomb oscillations. This is the regime of the “NT wire” in our measurements, where the charging energy, $\sim 1mV$, is small enough that the measurement temperature results in only weak gate-dependence of the conductance, and the series resistance to the metallic contacts nonetheless gives a small overall conductance. For a given overlap length of NT and contacts, when the temperature is low enough the leads would eventually show Coulomb blockade physics. For the device geometry shown in Fig. 2c such Coulomb physics of the leads is indeed seen at dilution temperatures (see section S6). However, by making the overlap with the contacts long

enough, and hence suppressing further the charging energy, it should be possible to make the leads behave as “wires” down to the lowest temperatures in our measurements.

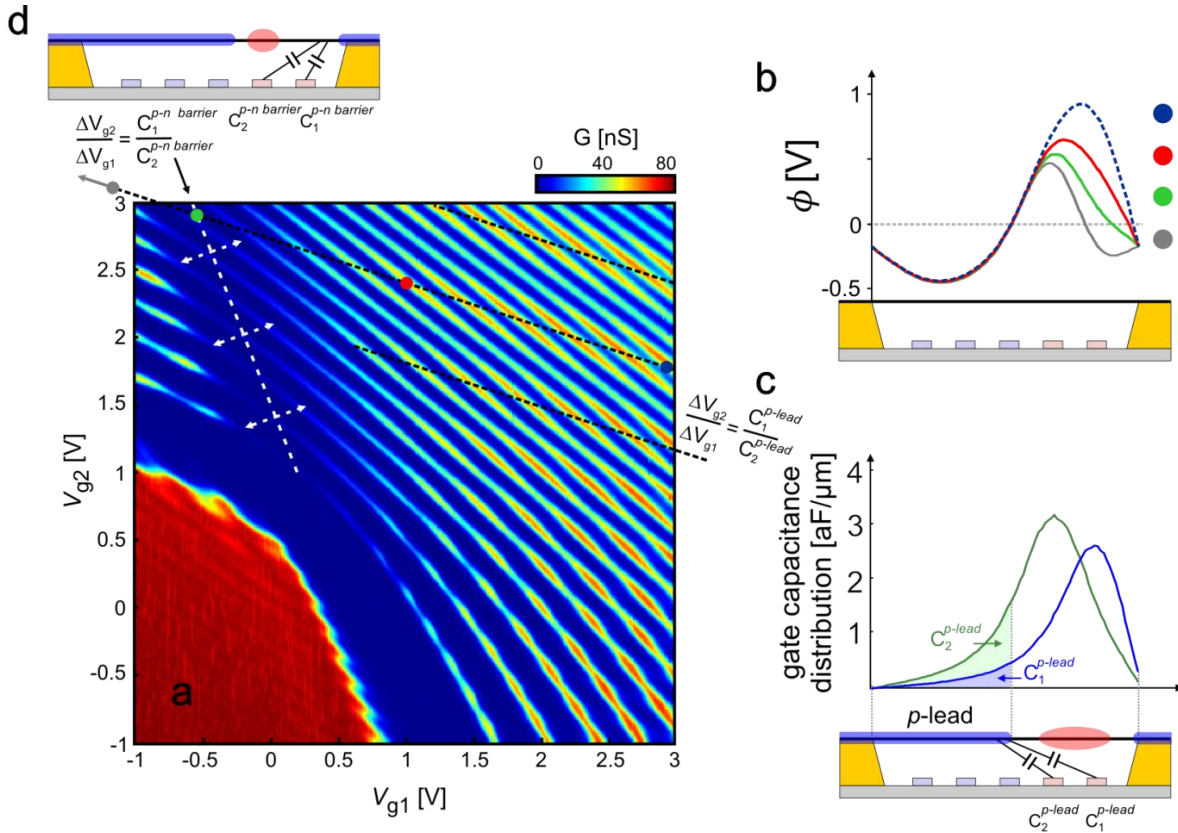


Figure S5: The electrostatic origin of the observed features in the two-gate conductance scans. a) The main panel (duplicating Fig. 3c of the main text) shows conductance, G , as a function of V_{g1} and V_{g2} while $V_{g3,5} = -0.8$ V. The dashed black lines and dashed white lines correspond to the secondary conductance features observed in this scan. These lines are drawn with slopes taken directly from the measured capacitances (see text and panels below). b) The electrostatic potential along the NT length, $\phi(x)$, calculated for the points indicated in panel a, with circle colors corresponding to line colors. The contact and gate work function differences are included as described in the text. The device schematic is to scale in both dimensions. c) Schematics of the electron (red) and hole (blue) population along the NT corresponding to the blue and red points in panel a. The top traces show the capacitance distributions of gates 1 and 2. The colored areas under the curves give the capacitances between these gates and the left NT hole “lead” to the dot. The ratio between these capacitance gives the slope of the dashed black lines in panel a d) Schematics of the electron and hole population along the NT corresponding to the green point in panel a. Here a dot forms only above gate 2 and the NT is in the gap over gate one. This leads to an extended right barrier that yields the suppression along the dashed white line in panel a. Its slope in the voltage-voltage plane is determined by the ration of the capacitances of the barrier region to gates 1 and 2.

S6. Designing electrostatic potentials with resolution determined by the gate pitch

In this section we demonstrate that with knowledge of the electrostatic coupling of the gates to the NT (as demonstrated in section S4 above), we can design potential profiles along the NT with a spatial resolution given by the gate pitch and not smeared by the separation between the NT and the gates. As explained in the main text, by distancing the nanotube from the gates, we preserve electron-electron interactions. But at the same time we also spatially smear the effect of individual gates on the NT. While a close gate controls the potential in the NT along a length comparable to its width, a distant gate affects a longer section amounting to the convolution of the gate width and its distance to the NT. This distance therefore reduces the effective resolution with which we can design electrostatic potentials. However, by using our knowledge of the non-local gate coupling, we can deconvolve this spatial smearing and define potential features whose sharpness is determined by the gate pitch alone. Such deconvolution works as long as the NT is not too far from the gates compared to the gate separation.

To define the potential (or the charge) on the NT with gate pitch resolution means that if we partition the NT into N segments of equal length, where N is the number of gates, we can define the potential (or charge) in each one of these segments independently. However, the charge on the i^{th} segment in the NT, q_i , due to a voltage on gate j , V_{gj} , is given by $q_i = C_{ij} \cdot V_{gj}$, where C_{ij} is the capacitance coupling matrix element. Thus, the above equation shows that a gate does not only affect the local segment above it but also neighboring segments, reducing the effective resolution. To define the charge on each segment independently, we instead *invert* the equation, $V_{gj} = C_{ji}^{-1} \cdot q_i$, to obtain the linear combination of gate voltages V_{gj} that is needed to control the charge in only a *single* segment of the NT, q_i . This inversion amounts to a discretized deconvolution of the capacitive smearing.

Figure S6 illustrates how this deconvolution works for the dimensions of our devices (a NT-gate distance of 130nm and a gate pitch of 150nm), using a calculation of the potential at the NT, $\phi(x)$, with Eq.S1, Applying a voltage on a single gate (Fig. S6a) leads to a potential along the NT spread out over ~325nm (Fig. S6b), roughly the sum of

the gate pitch and the NT-gate distance. On the other hand, if we use instead the linear combination of gate voltages found using the inverse capacitance matrix (Fig. S6c), we obtain a potential that is $\sim 160\text{nm}$ wide (Fig.S6d), comparable to the gate pitch. We note that the deconvolution becomes exponentially harder when the NT-gate distance becomes much larger than the gate pitch, $\eta \equiv \frac{d_{NT-gate}}{d_{gate-gate}} \gg 1$, since in this regime the voltages necessary for producing the desired potentials increase exponentially in η , and any experimental error in determining C_{ij} is exponentially amplified. However, as long as η is not very large, as in our experiments where $\eta \sim 1$, the above deconvolution procedure works well.

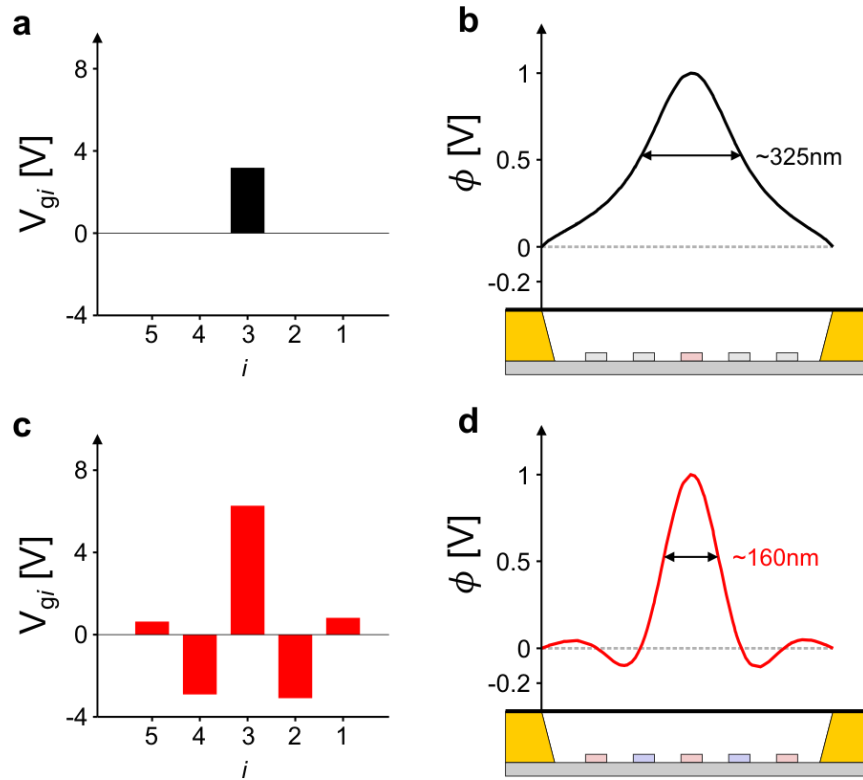


Figure S6: Recovering the gate resolution with potential design. a) The voltages applied on the gates and b) the corresponding calculated potential at the NT, $\phi(x)$, for the dimensions of our device (a NT-gate distance of 130nm and a gate pitch of 150nm). In this example a voltage is applied only on a single gate and the width of the potential feature along the NT is roughly the sum of the gate pitch and NT-gate distance. c) Linear combination of voltages for producing localized potential above the central gate, obtained by inverting the measured capacitance matrix. d) The corresponding calculated potential along the NT showing that the non-locality of the gate coupling can be effectively deconvolved.

S7. Transport data of a second device at dilution refrigerator temperatures

The device shown in the main text showed no observable indications of disorder at the energy scale of the measurement ($T = 4K$). A natural question is whether at lower temperatures, smaller disorder scales would become observable, and we address this with measurements at dilution refrigerator temperatures. Figure S6 shows the conductance of a five-gated device, different than the one shown in the main text, measured in a dilution refrigerator with a base temperature of $T = 7mK$ (extracted electron temperature is $T \approx 80mK$). At these temperatures, the device is expected to be sensitive to smaller magnitude disorder; we show in the following that our observations on device cleanliness hold to these low temperatures. For this experiment, the two right gates are biased together along the horizontal axis, $V_{g1} = V_{g2} = V_R$, the two left gates are biased together along the vertical axis, $V_{g4} = V_{g5} = V_L$, and the center gate is biased with the average voltage, $V_{g3} = (V_L + V_R)/2$.

Overall, this device demonstrates almost perfectly clean behavior. In the upper right (lower left) corners, we observe the creation of a five-gate electron (hole) dot (see corresponding schematics) with a single Coulomb oscillation periodicity. In the lower right and upper left corners, p - n junctions are formed at the center of the suspended NT, leading to the creation of a hole-electron and electron-hole double quantum dots respectively (see corresponding schematics). Notably, every vertical charging line in the lower right corner, corresponding to an electron localized on the right side of the device, evolves smoothly into a horizontal charging line in the upper left corner, corresponding to an electron localized on the left side. As explained in the main text this smooth evolution shows that individual electrons are smoothly shuttled from the right to the left side of the device without apparent effects of disorder. An almost perfectly symmetric behavior is observed for the hole charging lines that evolve smoothly from vertical in the top left corner to horizontal in the bottom right corner. One deviation from the perfect behavior is observed for the first hole line, which is vertical even on the bottom part of the gate-gate scan and does not bend like the others. This means that this hole gets stuck on the right side and is not shuttled to the left side by the gates. By checking the relative coupling of this feature to the individual gates (not shown) we see that it almost exclusively gated by

gate 5 and none of the others, demonstrating that this hole is localized between gate 5 and the contact. Such behavior could be due to a highly localized potential dip near the contact that binds only one carrier. Importantly, all the holes after this first localized one show the normal extended behavior and possess nearly perfect symmetry to the electrons.

Looking carefully on the data for the first few electrons and holes (excluding the first localized hole), we can observe small wiggles of the charging lines. These wiggles are an order of magnitude smaller than those observed in the best ultra-clean double-dot devices made to date², demonstrating that the underlying disorder potential in our devices is much smaller. As was clearly demonstrated², a potential hump or dip act differently on electron and holes, leading to different charging line structures for the two carrier types. The fact that we observe very similar wiggles for electrons and holes therefore emphasizes that disorder on the length scale of the gate spacing is probably not the mechanism leading to the observed wiggles. Instead, the effect must operate the same way on electrons and holes. One candidate is the attraction of the carriers in the NT to their image charges formed at the metallic leads, which leads to attractive potentials at the suspended NT edges for both electrons and holes, thereby leading to a double-dot-like effective potential which could explain the small wiggles. Another plausible mechanism is strong interactions between the carriers, which are predicted to lead to real-space separation of charge carriers and a similar modulation of the charging lines.

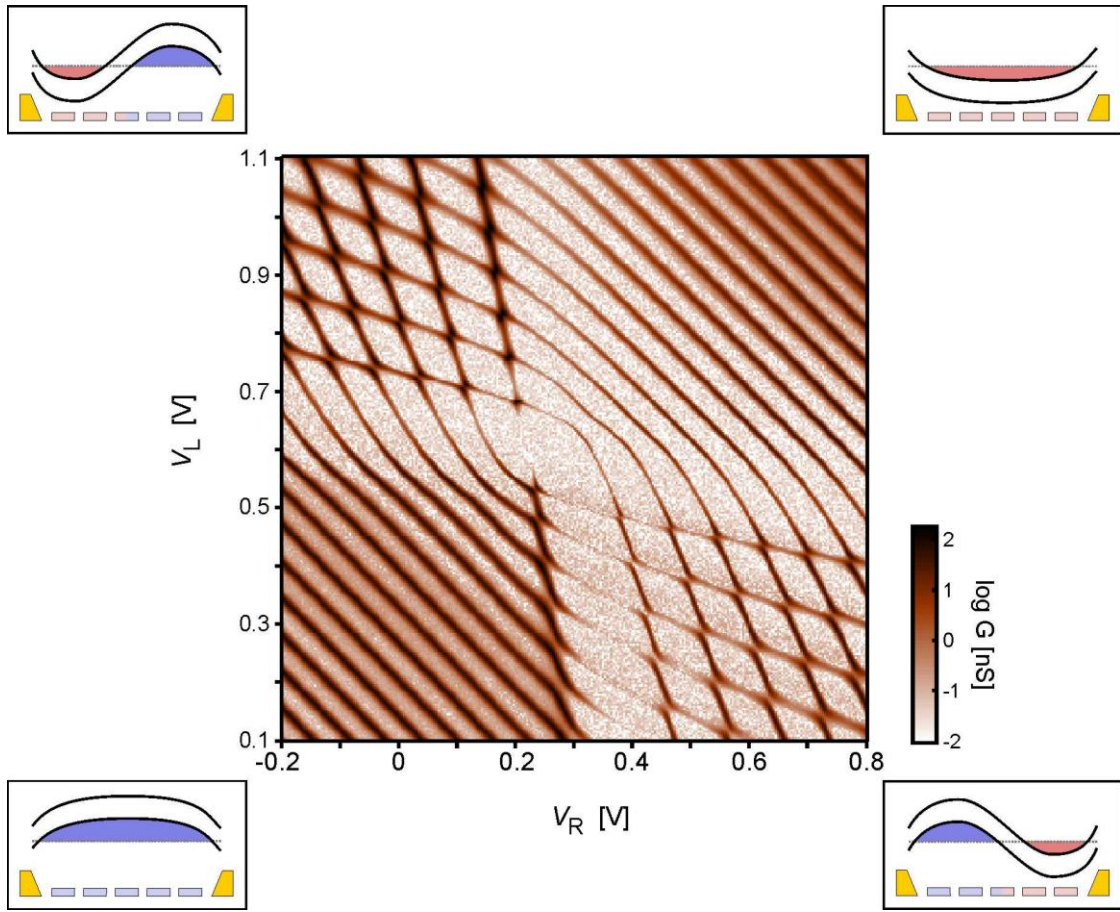


Figure S7: A second five-gated small bandgap NT device measured at dilution refrigerator temperatures. The conductance, G , on a logarithmic scale, measured as a function of right and left gate voltages, V_R and V_L . The right gate voltage is applied on the two right gates, $V_{g1} = V_{g2} = V_R$, the left gate voltage is applied on the two left gates, $V_{g4} = V_{g5} = V_L$ and on the center gate we apply the averaged value $V_{g3} = (V_R + V_L)/2$. The insets show schematic band diagrams corresponding to the four quadrants of the measurement: bottom left - a hole dot over all gates; top right - an electron dot above all gates; bottom right - electron/hole double dot; top left - hole/electron double dot.

S8. Electrical functionality of the two-NT device as a coupled system-detector

In the main text, we demonstrated the ability to place two nanotubes in the same device at a controlled separation (Fig.2d). This device geometry enables new device functionality: the ability to use one nanotube as a quantum-dot detector to electrically sense the second tube. This circuit implementation, new to suspended NTs, has a large number of potential applications, including: charge detection in ultra-clean 1D systems, charge measurement in quantum information implementations, and measurements of mechanical motion of NT nano-mechanical resonators. A few works in the past have incorporated local detectors into nanotube circuits^{3,4}, however, so far these devices have been limited to nanotubes lying on a substrate, and local detection of an ultra-clean suspended nanotube has remained a challenging goal. Here, we demonstrate the possibility to perform such detection in a suspended device using the simplest example, in which we use a quantum dot on one tube to electrically sense the mechanical oscillations of the second tube. This approach is reminiscent to the single electron transistor (SET) motion detection performed on bulk silicon nano-beams⁵, but here it is shown for the first time in the important context of multi-gated suspended nanotube. We note that due to the difficulty to make good SETs or quantum-dot detectors close to a NT mechanical resonator, to date, all studies of NT mechanical motion have used the gate-dependent transport through the moving NT itself to detect the motion. While this detection scheme has been very fruitful in past experiments⁶⁻¹¹, it puts important constraints on which measurements can be performed. Since the detection needs the transport through the resonator to be gate-dependent, it cannot be used, for example, when the transport is blockaded (e.g. within a Coulomb blockade valley) or conversely when it is in a ‘metallic wire’ regime having no gate dependence. Using an external quantum-dot detector to detect the movement, as we demonstrate below, decouples the mechanical and the detection components, alleviating the above constraints.

The measurement circuit is shown in figure S8. The left segment of the bottom NT, contacting the left and middle contacts and suspended above a single gate is used as the quantum-dot detector. A DC voltage on this local gate, V_g^{det} , creates a dot of electrons (marked red in the figure) and brings its Coulomb blockade transport to a point that is

sensitive to external gating. The top, longer NT forms the mechanical resonator, whose mechanical vibrations are measured using a simple adaptation of a standard mixing technique⁶: A frequency-modulated (FM) radiofrequency (RF) signal with a carrier frequency f is applied on the source contact of the detector quantum dot. This contact, being only 85nm away from the long NT, couples to it capacitively, actuating its mechanical motion when f is resonant with one of its mechanical modes. This motion, in turn, produces a fluctuating gate potential on the quantum-dot detector. The size of the oscillating gate potential produced by the mechanical motion is $\delta V_{elec} = \delta z_{mech} \frac{1}{C} \frac{dC}{dz} V_{res-det}$, where δz_{mech} is amplitude of the mechanical vibration, C and dC/dz are the capacitance between the resonator and detector NTs and its derivative with respect to their mutual distance, and $V_{res-det}$ is the (externally-controlled) bias between the resonator and detector circuits⁶. This oscillating gate signal is mixed down with the FM signal transmitted directly to the quantum dot by its source contact, through the finite transconductance of the dot's transport, $d^2I/dV_g dV_{sd}$, producing a low-frequency mixing current detected at its drain (middle contact) using a lock-in amplifier operating at the FM modulation frequency.

Figure S8b shows the out-of-phase component of the mixing current measured as a function of $V_{res-det}$ and f , at $T = 4\text{K}$. In addition to controlling the amplitude of the detected signal, the voltage difference $V_{res-det}$ applies also a mechanical force that tensions the long NT resonator. This tensioning leads to an increase of the frequencies of its mechanical modes. Fig. S8b shows one such mechanical resonance, visible as a peak in the mixing current, exhibiting a parabolic dependence of its frequency on $V_{res-det}$.

It is important to note that the above measurement was performed when the resonator NT was electrically tuned to be in the 'hole wire' regime, in which its transport is practically gate-independent. The absence of gate dependence would have not allowed the measurement of the mechanical resonance in the conventional way that uses transport through the resonator itself. However, such measurement becomes possible here by using the separate quantum-dot detector that can be tuned to a gate sensitive point, independent of the state of the resonator.

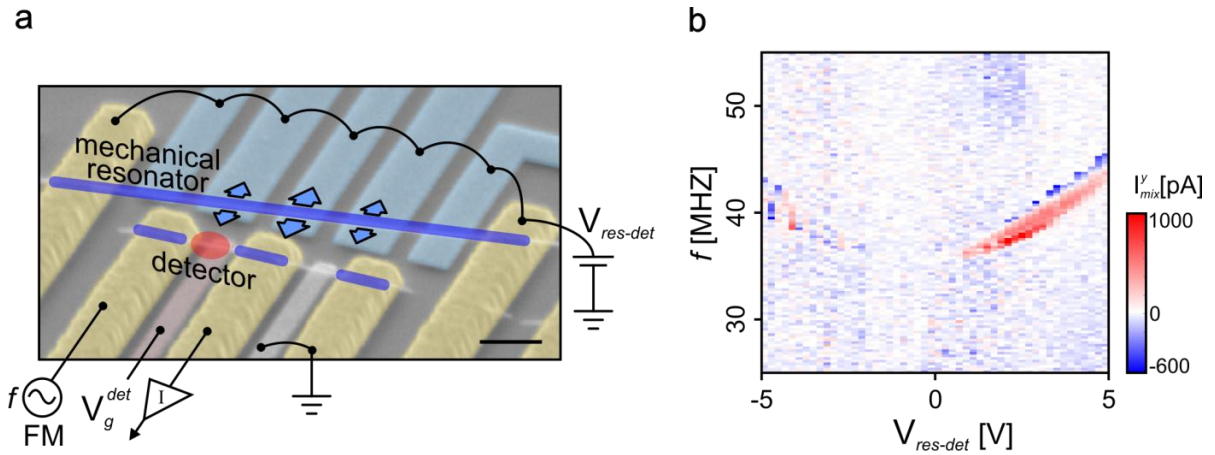


Figure S8: Electrical detection of a NT mechanical resonator motion using a second NT quantum dot detector. a) Measurement circuit, overlaid over the SEM image of the two-NT device from Fig. 2d of the main text, that was used in these measurements. Yellow: contacts. Blue/red/white: gates. The NTs are colored in red (blue) to reflect regions that are electron (hole) doped. The red blob represents a quantum dot formed on the left side of the bottom NT, suspended between two contacts, using a voltage on the gate beneath it, V_g^{det} . The second NT, doped with holes over its entire length, is driven into motion (indicated by blue arrows) by a frequency-modulated (FM) radiofrequency (RF) signal with a carrier frequency f applied on the left contact of the dot, that is capacitively coupled to it. The quantum dot acts as a non-linear mixing element, which mixes the RF signal on its source contact and the RF gating signal produced by the oscillating nanotube resonator, to a measurable low frequency signal measured at the drain of the dot (middle bottom contact). The right contact and gate are grounded during the measurement. The contacts and gates of the resonator tube are all kept at the same potential, $V_{res-det}$, which we control. Scale bar $300nm$. b) The out-of-phase component of the mixing current, I_{mix}^y (colormap), measured as a function of the bias between the resonator and detector circuits, $V_{res-det}$, and the FM carrier frequency f . The signal vanishes everywhere except at a mechanical resonance of the resonator, whose frequency increases with increasing $V_{res-det}$ due to electrostatic tensioning of the NT resonator.

References

1. Liang, W. *et al.* Fabry - Perot interference in a nanotube electron waveguide. *Nature* **411**, 665–9 (2001).
2. Steele, G. a, Gotz, G. & Kouwenhoven, L. P. Tunable few-electron double quantum dots and Klein tunnelling in ultraclean carbon nanotubes. *Nature nanotechnology* **4**, 363–7 (2009).
3. Gotz, G., Steele, G. a, Vos, W.-J. & Kouwenhoven, L. P. Real time electron tunneling and pulse spectroscopy in carbon nanotube quantum dots. *Nano letters* **8**, 4039–42 (2008).
4. Churchill, H. O. H. *et al.* Relaxation and Dephasing in a Two-Electron C13 Nanotube Double Quantum Dot. *Physical Review Letters* **102**, 2–5 (2009).
5. Naik, a *et al.* Cooling a nanomechanical resonator with quantum back-action. *Nature* **443**, 193–6 (2006).
6. Sazonova, V. *et al.* A tunable carbon nanotube electromechanical oscillator. *Nature* **431**, 284–7 (2004).
7. Witkamp, B., Poot, M. & Van der Zant, H. S. J. Bending-mode vibration of a suspended nanotube resonator. *Nano letters* **6**, 2904–8 (2006).
8. Peng, H., Chang, C., Aloni, S., Yuzvinsky, T. & Zettl, a. Ultrahigh Frequency Nanotube Resonators. *Physical Review Letters* **97**, 087203 (2006).
9. Lassagne, B., Aguasca, A. & Bachtold, A. Ultrasensitive Mass Sensing with a Nanotube Electromechanical Resonator. *Nano letters* **2**, 4–7 (2008).
10. Wang, Z. *et al.* Phase transitions of adsorbed atoms on the surface of a carbon nanotube. *Science (New York, N.Y.)* **327**, 552–5 (2010).
11. Wu, C. C., Liu, C. H. & Zhong, Z. One-step direct transfer of pristine single-walled carbon nanotubes for functional nanoelectronics. *Nano letters* **10**, 1032–6 (2010).